

Parametric analysis of thermal behavior during selective laser melting additive manufacturing of aluminum alloy powder



Yali Li, Dongdong Gu *

College of Materials Science and Technology, Nanjing University of Aeronautics and Astronautics, Yudao Street 29, Nanjing 210016, PR China

Institute of Additive Manufacturing (3D Printing), Nanjing University of Aeronautics and Astronautics, Yudao Street 29, Nanjing 210016, PR China

ARTICLE INFO

Article history:

Received 12 May 2014

Accepted 3 July 2014

Available online 10 July 2014

Keywords:

Additive manufacturing

Selective laser melting

Numerical simulation

Thermal behavior

Aluminum alloy

ABSTRACT

Simulation of temperature fields during selective laser melting (SLM) additive manufacturing of AlSi10Mg powder was performed using the finite element method (FEM). The effects of laser power and scan speed on the SLM thermal behavior were investigated. It showed that the cooling rate of the molten pool elevated slightly from 2.13×10^6 °C/s to 2.97×10^6 °C/s as the laser power increased from 150 W to 300 W, but it enhanced significantly from 1.25×10^6 °C/s to 6.17×10^6 °C/s as the scan speed increased from 100 mm/s to 400 mm/s. The combination of a low laser power (200 W) and a high scan speed (400 mm/s) yielded a low temperature (1059 °C) and an extremely short liquid lifetime (0.19 ms), resulting in the poor wettability and occurrence of micropores in SLM-produced parts. The temperature gradient along the depth direction of the molten pool increased considerably from 10.6 °C/μm to 21.7 °C/μm as the laser power elevated from 150 W to 300 W, while it decreased slightly from 14.9 °C/μm to 13.5 °C/μm as the scan speed increased from 100 mm/s to 400 mm/s. The proper molten pool width (111.4 μm) and depth (67.5 μm) were obtained for a successful SLM process using the laser power of 250 W and scan speed of 200 mm/s. SLM of AlSi10Mg powder was also experimentally performed using different laser processing conditions and the microstructures of the SLM-fabricated samples were investigated to verify the reliability of the physical model. A sound metallurgical bonding between the neighboring fully dense layers was achieved at laser power of 250 W and scan speed of 200 mm/s, due to the larger molten pool depth (67.5 μm) as relative to the layer thickness (50 μm).

© 2014 Elsevier Ltd. All rights reserved.

1. Introduction

Due to the attractive combination of excellent weldability, high heat conductivity, sufficient harden ability and good corrosion resistance, aluminum alloys have been widely used in various areas, such as automotive, aerospace and domestic industries [1,2]. Among them, some aluminum alloy parts are normally in complex and irregular configurations, which are difficult to fabricate using the conventional processing methods such as casting processes. Furthermore, the coarsened microstructures and the large degrees of segregation would be generated due to the slow solidification rates during the conventional casting processes [3]. Therefore, new processing methods are highly demanded to satisfy the need for obtaining complex components with fine and uniform microstructures.

Selective laser melting (SLM), as one of the newly developed additive manufacturing (AM) techniques, exhibits a great potential

for direct fabricating three-dimensional parts with complex structures [4–7]. During the SLM process, the part is fabricated by selectively melting and consolidation of thin layers of powder using a scanning laser beam according to the CAD data of the part. As a high-energy laser beam is scattered on the powder layer, the energy is absorbed by powder particles via both bulk-coupling and powder-coupling mechanisms [8]. The transient temperature field with a high temperature (up to 10^5 °C) and a rapid cooling rate (up to 10^{6-8} °C/s) is formed during the interaction between the laser beam and the powder bed [9,10], which has a substantial effect on the microstructures and resultant mechanical properties of the final component. The transient thermal behavior during the SLM process is controlled considerably by the processing parameters, such as laser power and scan speed. In fact, due to the complex metallurgical nature of SLM, which involves multiple modes of heat, mass, and momentum transfer, the typical defects associated with SLM such as “balling effect”, pores and thermal cracks tend to occur under the inappropriate processing conditions [11,12]. Therefore, to obtain the desired SLM-fabricated parts, the significant research efforts are required to study the relationship

* Corresponding author. Tel./fax: +86 25 52112626.

E-mail address: dongdonggu@nuaa.edu.cn (D. Gu).

Nomenclature

A	laser energy absorptance of a material	R	effective radius of laser beam, m
c	specific heat capacity, J/(kg·°C)	r	radial distance from a point to the center of the laser beam, m
H	enthalpy, J/m ³	T	temperature of the powder system, °C
h	coefficient of heat convection, W/(m ² °C)	T_m	melting temperature, °C
k	thermal conductivity, W/(m °C)	T_0	ambient temperature, °C
k_p	thermal conductivity of powder bed, W/(m °C)	t	interaction time, s
k_s	thermal conductivity of solid, W/(m °C)	x, y, z	coordinates, m
n	normal vector	ε	emissivity
P	laser power, W	ρ	density, kg/m ³
Q	heat generation per volume, W/m ³	σ	Stefan–Boltzmann constant
q	input heat flux, W/m ²	φ	porosity
q_c	heat convection, W/m ²		
q_r	heat radiation, W/m ²		

between processing parameters and thermal behavior. However, the experimental measurements of thermal behavior during the SLM process are considered to be difficult since it involves the localized heating and superfast melting and solidification. Consequently, the numerical simulation approach is chosen as a typically alternative to solve these problems.

In fact, some heat conduction models have been established to investigate the thermal behavior during the SLM process in the past. Roberts et al. [13] predicted the transient temperature field for TiAl6V4 powder layers of parts produced by the SLM process. The results indicated that the laser heated regions experienced rapid thermal cycles, which would be accompanied by commensurate thermal stress cycles. Childs and Hauser [14] developed a 3D model to study the relationship between the processing parameters and the masses of the H13 tool steel powder layers during the SLM process. It suggested that the thermal history of processing is influential in determining the amount of melt under a laser beam at any instant during processing. Gusarov et al. [15–17] numerically calculated and analyzed the temperature distribution of steel 316L powder bed during the SLM process. It was found that the stability of the process was highly dependent on the scan speed, powder layer thickness, and the thermal properties of materials. Zhang and co-workers [18–20] established a three-dimensional model for laser sintering of two-component metal powder to achieve the best combination of processing parameters. They paid attention to the influence of the moving heat source intensity, the scan speed, and the thickness of the powder layer on both the configuration of the heat affected zone and temperature distribution.

Although there are some numerical simulations have been carried out to investigate the thermal behavior during laser processing of metal powders, the limited researches focus on the thermal behavior during SLM of AlSi10Mg powder. Meanwhile, due to the high reflectivity and high thermal conductivity of AlSi10Mg powder, the SLM of AlSi10Mg powder process is difficult to control compared with producing other metal powders such as stainless steels or titanium alloys [1]. Therefore, a further understanding regarding the SLM of AlSi10Mg powder process needs to be necessarily developed. In this investigation, the three-dimensional finite element model was developed to predict the relationship between processing parameters and thermal behavior during SLM of AlSi10Mg powder, using the ANSYS 12.0 commercial finite element method (FEM) software. The effects of laser power (P) and laser scan speed (v) on the thermal behavior and the configurations of molten pool were preliminary analyzed. Moreover, corresponding experiments were also implemented to study the microstructure of the SLM-produced components under different laser

processing conditions, in order to verify the reliability of the physical model.

2. Model for SLM process

2.1. Physical description of the model

Fig. 1 depicts the schematic diagram of SLM process. As the laser beam irradiated the top surface of the powder bed, a fraction of laser energy was reflected and the remainder was absorbed. The absorbed laser energy melted the powder, thereby yielding a small-sized molten pool. The metallurgical bonding was formed between the adjacent tracks and the neighboring layers as the solidification occurred. During the process, besides the consideration of the thermal conduction, the heat losses due to convection and radiation should also be taken into account, in order to make a correct description of the thermal behavior.

The spatial and temporal distribution of the temperature field satisfies the differential equation of 3D heat conduction in a domain D , which can be expressed as [21,22]:

$$\rho c \frac{\partial T}{\partial t} = \frac{\partial}{\partial x} \left(k \frac{\partial T}{\partial x} \right) + \frac{\partial}{\partial y} \left(k \frac{\partial T}{\partial y} \right) + \frac{\partial}{\partial z} \left(k \frac{\partial T}{\partial z} \right) + Q \quad (1)$$

where ρ is the material density, c is the specific heat capacity, T is the temperature of the powder system, t is the interaction time, k is the thermal conductivity, and Q is heat generated per volume within the component.

The initial condition of the temperature distribution in the powder bed at time $t = 0$ can be defined as:

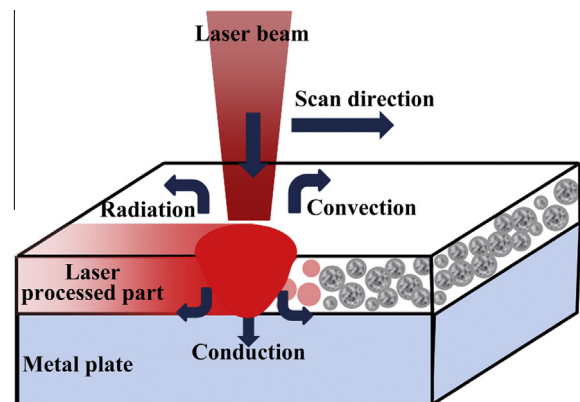


Fig. 1. Schematic of thermal behavior of powder bed under laser irradiation.

$$T(x, y, z, t)|_{t=0} = T_0 \quad (x, y, z) \in D \quad (2)$$

where T_0 is the ambient temperature and is taken as 20 °C.

The natural boundary condition can be expressed as [23]:

$$k \frac{\partial T}{\partial n} - q + q_c + q_r = 0 \quad (x, y, z) \in S \quad (3)$$

where S represents the surfaces which are attached to imposed heat fluxes, convection and radiation, n is the normal vector of surface S , the input heat flux q is presented in the following by Eq. (6), q_c is the heat convection and can be defined by:

$$q_c = h(T - T_0) \quad (4)$$

q_r is the heat radiation and can be expressed by:

$$q_r = \sigma \varepsilon (T^4 - T_0^4) \quad (5)$$

In Eqs. (4) and (5), h is the coefficient for heat convection, σ is the Stefan–Boltzmann constant, and ε is the emissivity.

2.2. Basic setup of the finite element model

Numerical simulation was performed using the ANSYS Multi-physics finite element package. The finite element model and laser scanning pattern during the SLM process are present in Fig. 2. The laser scan area on the AlSi10Mg powder bed had a length of 1.54 mm, a width of 0.7 mm and a thickness of 0.1 mm. The C45 medium carbon steel block with the dimensions of 2 mm × 1 mm × 0.4 mm was taken as the substrate for the powder bed. Considering the calculation efficiency and the computational precision, the solid 70 hexahedron elements with the fine mesh of 0.0175 mm × 0.0175 mm × 0.025 mm were used in the powder bed, while a relatively coarse tetrahedron mesh was adopted in the

Table 1

Thermal physical parameters of solid AlSi10Mg [28,29].

Temperature, T (°C)	20	100	200	300	400
Thermal conductivity, k_s (W/m °C)	147	155	159	159	155
Specific heat capacity, c (J/kg °C)	739	755	797	838	922
Density, ρ (kg/m ³)	2650				

substrate. The three-dimensional simulation model was meshed into 53994 elements and 23914 nodes. The laser beam moved in a reciprocating raster pattern and the applied laser processing parameters are shown in Table 1.

In the present model, some assumptions were made as follows:

- (1) The whole AlSi10Mg powder bed was assumed to be a continuous and homogeneous media.
- (2) During the melting process, the thermal physical parameters of the material such as thermal conductivity and specific heat capacity were considered to be temperature-dependent.
- (3) The coefficient of convection between the AlSi10Mg powder bed and the environment was assumed to be a constant.
- (4) The moving laser heat source acting on the AlSi10Mg powder bed was modeled as the Gaussian distribution of heat flux and was input directly on the surface of the powder layer.

2.3. Design of Gaussian heat source model

During the SLM process, the induced fusion of material was usually achieved using a laser beam as a thermal energy source. The distribution of the laser intensity followed nearly a Gaussian relationship, which was mathematically presented as [24]:

$$q = \frac{2AP}{\pi R^2} \exp\left(-\frac{2r^2}{R^2}\right) \quad (6)$$

where P is the laser power, R denotes the effective laser beam radius at which the energy density reduced to its $1/e^2$ at the center of the laser spot, and r is the radial distance from a point on the powder bed surface to the center of the laser spot, and A is laser energy absorptance of a material affected by the wavelength of laser, the surface conditions and the physical properties of the material. The absorptance of 9% for aluminum at the Nd:YAG wavelength (1.06 mm) irradiations came from Louvis et al.'s work [25].

Considering the melting and solidification phenomenon that occurred in the SLM process, the latent heat could not be negligible for the phase change. To define the latent heat, the enthalpy was expressed as a function of temperature:

$$H = \int \rho c dT \quad (7)$$

where ρ is the material density, c is the specific heat capacity, and T is the temperature of the molten pool formed in the powder bed.

2.4. Determination of thermal physical parameters

The effective thermal conductivity of a loose powder bed is an important material property determining the accuracy of the simulation results of SLM. Rombouts et al. [26] found that the effective thermal conductivity of a powder bed was controlled by the gas filling pores and was also depended on the solid fraction and the particle size. Thummler and Oberacker [27] proposed that the effective thermal conductivity of the powder bed can be represented by a simplified generic relationship

$$k_p = k_s(1 - \phi) \quad (8)$$

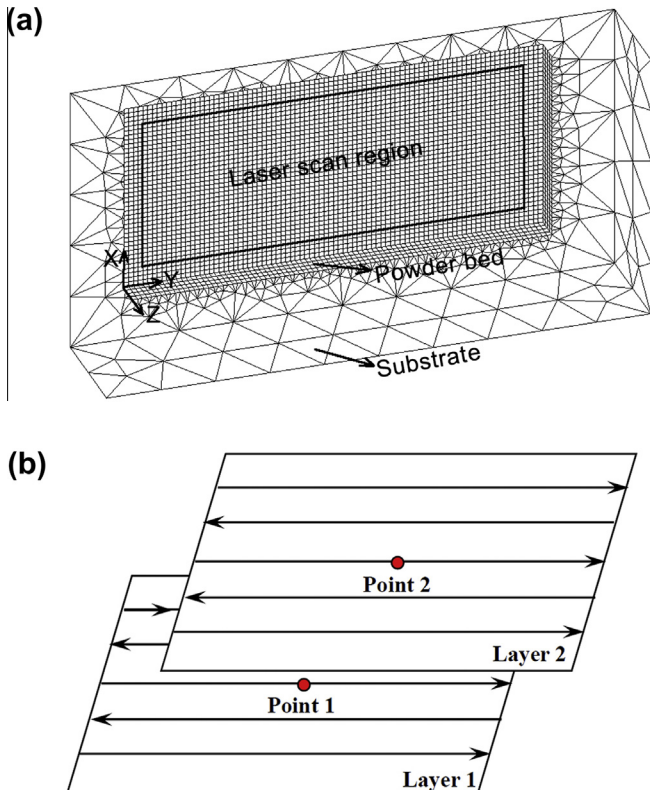


Fig. 2. (a) Finite element model and (b) laser scanning pattern during SLM process (point 1: at the center of the first layer; point 2: at the center of the second layer).

where k_p and k_s are the thermal conductivities of powder bed and solid materials, and ϕ is the porosity of the powder bed which can be written as [22]:

$$\phi = \frac{\rho_s - \rho_p}{\rho_s} \quad (9)$$

where ρ_s and ρ_p are the densities of the solid and powder materials, respectively. Normally, the porosity is assumed to vary from $\phi = 0.40$ for powder state to $\phi = 0$ for solid state.

In the present model, AlSi10Mg was selected as the simulation material in an initial solid powder state, which was then fused by the scanned laser beam. It should be noted that the powder thermo-physical properties were then changed as the powder temperature exceeded its melting point during the laser radiation process. The variation of thermophysical properties of solid AlSi10Mg with temperature is shown in Table 1 [28,29].

3. Experimentation

The 99.7% purity AlSi10Mg powder with a spherical shape and an average particle size of $\sim 30 \mu\text{m}$ was used in this study. The SLM apparatus as used mainly consisted of a YLR-500-SM ytterbium fiber laser with a output power of $\sim 500 \text{ W}$ and a spot diameter of $70 \mu\text{m}$, a computer control system for SLM process, and an automatic system for powder delivery. The entire SLM process was conducted in argon atmosphere. The processing parameters in the experiments were same as those used in the simulations (Table 2). Samples for metallographic examinations were cut, ground and polished according to standard procedures. The cross-sectional microstructures of the SLM-fabricated AlSi10Mg parts were characterized using a PMG3 optical microscopy (Olympus Corporation, Japan). The characteristic surface morphologies of the SLM-fabricated AlSi10Mg parts were characterized by a Quanta 200 scanning electron microscopy (SEM) (FEI Company, The Netherlands) in secondary electron mode at 20 kV .

4. Results and discussion

4.1. Characteristics of temperature distributions

Fig. 3 shows the transient temperature distribution on the top surface and cross-section of the molten pool as the laser beam reaches different layers during the SLM process, using P of 250 W and v of 200 mm/s . At the center of the first powder layer (point 1, Fig. 2), the isotherm curves on the top surface of the molten pool were similar to a series of ellipses. Moreover, the isotherm curves were intensive at the fore part of the ellipses compared with those at the back-end of it. The dashed line circle presented the isotherm of the melting temperature of AlSi10Mg (600°C). The area inside the black isotherm line possessed higher temperature than that of the melting temperature of AlSi10Mg, which induced a small molten pool within this area. The predicted working temperature of the molten pool decreased gradually from 1482°C in the center of the molten pool to 535°C at the edge of the pool. The width of

the molten pool was approximately $94.2 \mu\text{m}$ (Fig. 3a), while the length and depth of which were approximately $129.1 \mu\text{m}$ and $61.7 \mu\text{m}$, respectively (Fig. 3b). As the laser beam reached the center of the second layer (point 2, Fig. 2), the operative SLM temperature of the molten pool ranged from 1548°C in the center to 664°C at the edge of the pool. The width of the molten pool ($111.4 \mu\text{m}$) increased by 15.4% compared to that in the first layer (Fig. 3c). The length ($148.3 \mu\text{m}$) and depth ($67.5 \mu\text{m}$) of the molten pool were also slightly larger than those in the first layer, increasing by 12.9% and 8.5% , respectively (Fig. 3d).

From the simulation results, it can be seen that the isotherm curves arrange more intensive at the fore part of the ellipses (unscanned zone) than that at the back-end of the ellipses (scanned zone). This is mainly due to the change of thermal conductivity caused by the transition from powder to solid, which in turn contributes to heat transmission in the powder layer. During the SLM process, as the laser beam moves from the first layer to the second layer, the average temperature and the size of the molten pool increase gradually. This is considerably attributed to the fact that the heat stored in the previous layer has an influence on the next processing layer and, accordingly, resulting in the heat accumulation effect in SLM process. Moreover, it is known that the energy losses through the conduction are higher than convection/radiation during the laser process. With the development of shaped layers, the heat dissipation by conduction relatively becomes less dominant than the heat dissipation by convection/radiation, resulting in the decrement of energy losses [30]. This behavior leads to a higher temperature and a larger molten pool.

4.2. Thermal behaviors

Fig. 4 shows the temperature variation with time at the center of the first layer (point 1, Fig. 2) during the SLM of AlSi10Mg powder process, using different v and different P . The curve slope denotes the cooling rate of point 1. The temperature distribution showed an apparent fluctuation behavior and each peak represented a laser beam pass. The temperature rose up rapidly as the laser beam approached and decreased sharply as the laser beam moved away, which accordingly gave rise to a high cooling rate during the SLM process. The third peak temperature was highest due to the arrival of the laser beam at point 1. As the P increased from 150 W to 300 W , the maximum cooling rate of point 1 increased monotonously from $2.13 \times 10^6^\circ\text{C/s}$ to $2.97 \times 10^6^\circ\text{C/s}$. Meanwhile, the maximum temperature of point 1 elevated dramatically from 887°C to 1754°C at 17.2 ms , which has surpassed the melting point of AlSi10Mg (600°C) (Fig. 4a, Fig. 4b). The eighth peak temperature of point 1, as the laser beam scanned over the second layer, was apparently above 600°C for the usage of P larger than 200 W (Fig. 4a). This indicated the occurrence of remelting phenomenon in the first layer and the resultant good metallurgical bonding ability between the adjacent layers. Similarly, as the applied v increased from 100 mm/s to 400 mm/s , the maximum cooling rate of point 1 increased considerably from $1.25 \times 10^6^\circ\text{C/s}$ to $6.17 \times 10^6^\circ\text{C/s}$. The maximum temperature of point 1, however, decreased considerably from 1354°C to 1032°C . For the applied v less than 200 mm/s , the eighth peak temperature of point 1 was still higher than the AlSi10Mg melting line as the laser beam scanned over the second layer (Fig. 4c). In other words, remelting phenomenon occurred in the first processed layer owing to the sufficient energy penetration of the laser beam.

As the layer-by-layer melting process continues, the temperature distribution in the powder layer becomes complicated, due to the complex iteration behavior of heating and cooling. On the other hand, the applied P and v both play key roles in influencing the thermal behavior within SLM process. Based on the simulation results, it is reasonable to conclude that the cooling rate of the

Table 2
Finite element simulation parameters.

Parameter	Value
Absorptivity, A	0.09
Powder layer thickness, d	$50 \mu\text{m}$
Laser spot size, D	$70 \mu\text{m}$
Hatch spacing, s	$50 \mu\text{m}$
Ambient temperature, T_0	20°C
Laser power, P	$150, 200, 250, 300 \text{ W}$
Scan speed, v	$100, 200, 300, 400 \text{ mm/s}$

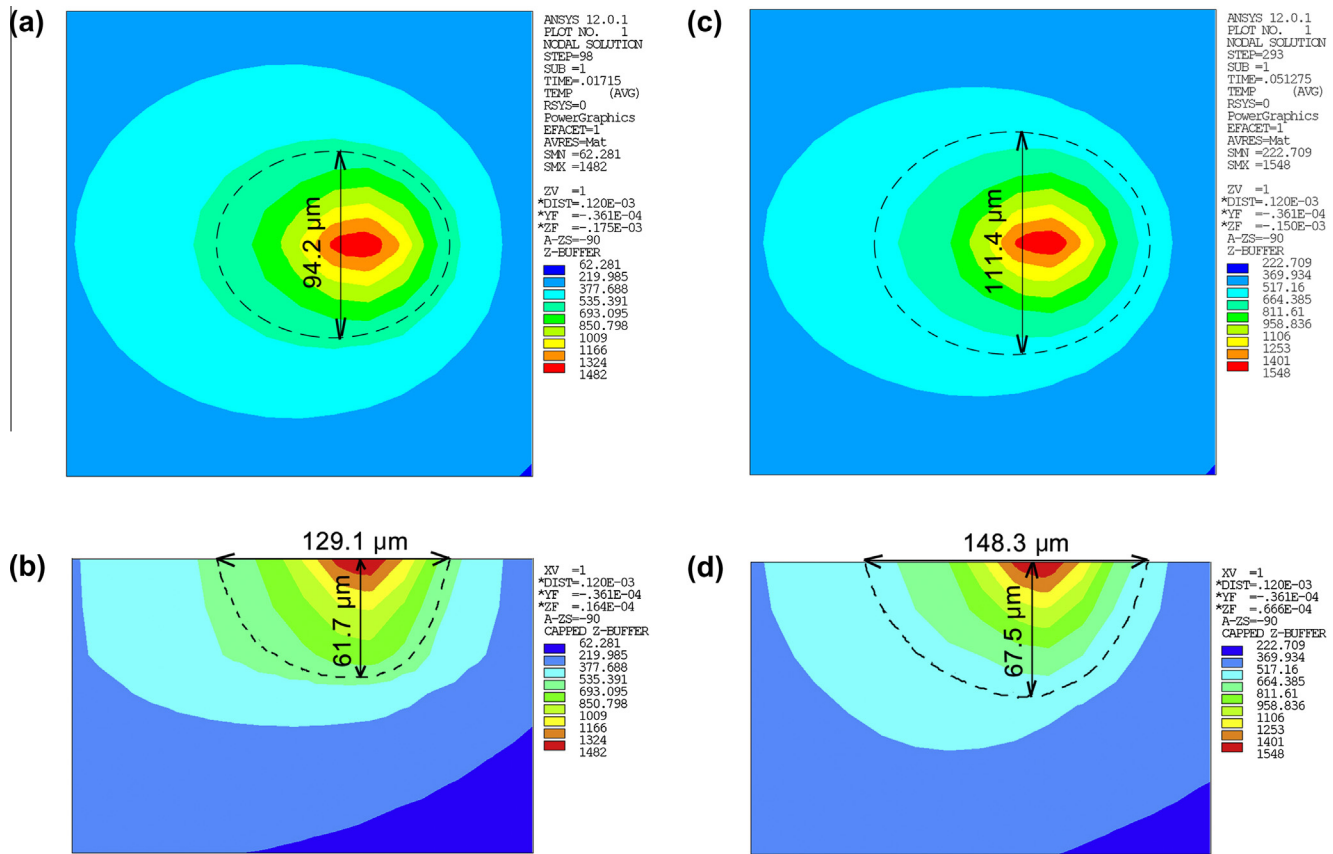


Fig. 3. Temperature distributions during SLM process at $P = 250$ W and $v = 200$ mm/s: (a) on the top surface of the molten pool as the laser beam reached the center of the first layer (point 1); (c) on the top surface of the molten pool and (d) on the cross-section of the molten pool as the laser beam reached the center of the second layer (point 2).

molten pool elevates with the increase of the applied P and v . Furthermore, it revealed that the cooling rate is more sensitive to the applied v than the P . At a relatively higher v of 400 mm/s, the occurrence of large thermal gradients induced by higher cooling rate tends to increase the residual stresses, which in turn resulting in an increment of cracking susceptibility. It should also worth noting that when a relatively low v (100 mm/s) is applied, the combination of the lower cooling rate (1.25×10^6 °C/s) and higher temperature (1354 °C) may be detrimental to the refinement of microstructure and resultant mechanical properties of the final component [31].

Fig. 5 shows the variation in the maximum temperature and the liquid lifetime at the center of the second layer with variations of P and v (point 2). It can be clearly seen that the maximum temperature and the liquid lifetime were generally linear to the applied P . When the applied P increased from 150 W to 300 W, the maximum temperature enhanced considerably from 937 °C to 1817 °C as a result of the higher laser energy density input. Meanwhile, the liquid lifetime prolonged from 0.32 ms to 1.04 ms (Fig. 5a). On the other hand, elevating the applied v from 100 mm/s to 400 mm/s resulted in the sharply decrement of the maximum temperature from 1483 °C to 1059 °C. Accordingly, the liquid lifetime also shortened considerably from 1.93 ms to 0.19 ms. Furthermore, it should be noted that the decreasing tendency in the maximum temperature and the liquid lifetime became moderate as the applied v increased above 200 mm/s (Fig. 5b).

The AlSi10Mg powder particles start to melt as the input laser energy is sufficient to yield a high-temperature molten pool during the SLM process. Meanwhile, the AlSi10Mg physical parameters also vary due to the powder–liquid phase change phenomenon,

which contributes to the heat transmission within the layer structure. As the applied P increases or v decreases, the amount of energy absorbed by the powder elevates under the function of laser irradiation, leading to a considerably longer liquid lifetime. It should be noted that an excessive increase in the P (300 W) or decrease in the v (100 mm/s) probably result in a relatively larger molten pool consisting of AlSi10Mg liquid with the higher thermal conductivity, which in turn increases the temperature of the entire powder bed system. The significant heat accumulation effect thus occurs, resulting in a sharp decrease of the obtained melt viscosity due to the markedly increased temperature. In this situation, the “balling” effect, which is a typical metallurgical defect associated with the powder-bed-based SLM process, is likely to occur, due to the high capillary instability of the melt in the pool [32–34]. On the other hand, for a relatively low P (150 W) or a high v (400 mm/s), the insufficient laser energy input to the powder layer yields a low temperature and an extremely short liquid lifetime. Consequently, a small amount of liquid with a high melt viscosity may be formed, thus decreasing the wetting characteristics of the melt within the pool and probably resulting in the formation of micropores in the SLM-produced part [35].

Fig. 6 shows the temperature gradient along depth direction (Z -direction) of the molten pool using different P and different v during SLM of AlSi10Mg. The temperature gradient decreased monotonously from the top of the molten pool ($Z = 0$) to the bottom of processed powder bed ($Z = 0.1$ mm). When the applied P increased from 150 W to 300 W, the maximum temperature gradient varied significantly, increasing from 10.6 °C/μm to 21.7 °C/μm (Fig. 6a). The temperature gradient increased linearly with the enhancement of the applied P . However, as the v

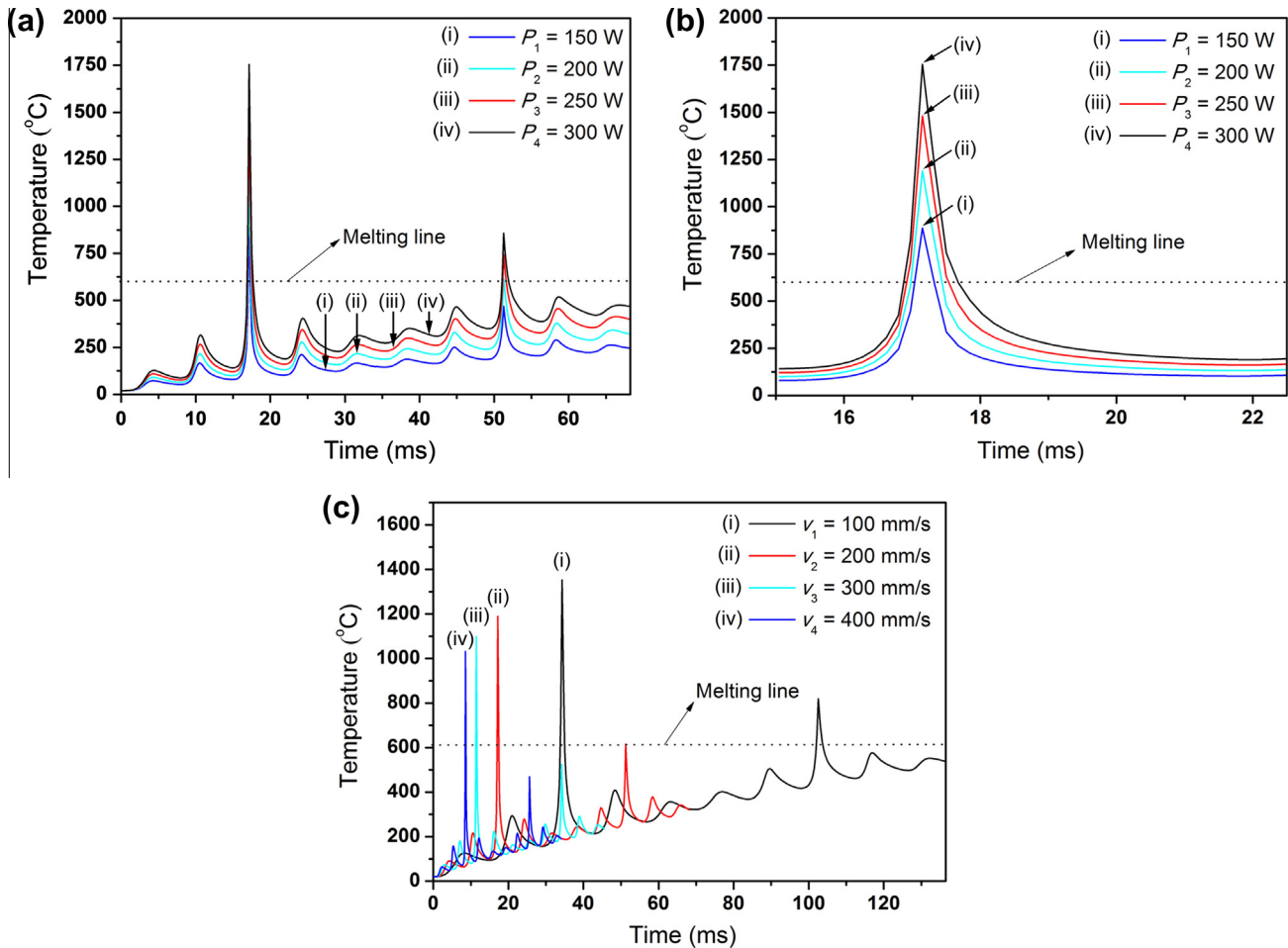


Fig. 4. The temperature variation with time at the center of the first layer (point 1) during SLM of AlSi10Mg powder process: (a) using different laser powers ($v = 200$ mm/s); (b) the local enlargement of (a) from 15 ms to 22.3 ms and (c) using different laser scan speeds ($P = 200$ W).

increased from 100 mm/s to 400 mm/s, the maximum temperature gradient decreased slightly from $14.9^\circ\text{C}/\mu\text{m}$ to $13.5^\circ\text{C}/\mu\text{m}$ (Fig. 6b). The simulation results illustrated that there was a slight decrease in the temperature gradient with the increase in v during SLM of AlSi10Mg powder.

Based on the calculated results in Fig. 6, it is reasonable to conclude that the variation of the temperature gradient in the molten pool along the Z-direction is considerably pronounced as the applied P increases. On increasing the applied P to 300 W, the maximum temperature gradient ($21.7^\circ\text{C}/\mu\text{m}$) may lead to the formation of large thermal stress. Thermal cracks and/or deformation thus tend to occur in the SLM-processed parts due to the release of the stresses [36]. A careful comparison of the data in Fig. 6b and d revealed that the temperature gradient in the molten pool along the Z-direction was considerably sensitive to the applied laser power than laser scan speed. This mainly because the temperature of AlSi10Mg powder bed is controlled directly by the applied P during the SLM process, while the applied v affects the temperature by changing the interaction time between the laser beam and AlSi10Mg powder bed. As the distance from the top of the molten pool increases, the temperature gradient gradually decreases. During the SLM process, the heat is mainly dissipated through the previously fabricated layer [37]. The solidified AlSi10Mg material in the previously fabricated layer has the higher thermal conductivity compared to the melt AlSi10Mg material in the molten pool, which accordingly gives rise to a decrease in the temperature gradient along the Z-direction.

4.3. Molten pool configurations

Fig. 7 shows the change of cross-sectional temperature contours and the length to depth ratio of molten pool with variation of P . The zone encompassed by the black dashed line (600°C) depicted the molten pool, while the length and depth of which were specifically noted in the temperature contours. At a lower P of 150 W, a small molten pool was produced with a length value of $64.3\ \mu\text{m}$ and depth of $33.7\ \mu\text{m}$. In this circumstance, the length to depth ratio was calculated to be 1.91 (Fig. 7e). The isotherm curves were found to be regularly and closely spaced within the molten pool, which exhibited an opposite trend outside the molten pool (Fig. 7a). For the case with a higher P of 200 W, the respective length and depth of the molten pool increased by 38.0% and 32.8% (Fig. 7b), leading to the length to depth ratio increased to 2.07 (Fig. 7e). Moreover, the distribution of the isotherm curves was found to be similar to that of 150 W. On increasing the applied P to 250 W, the molten pool with length of $148.3\ \mu\text{m}$ and depth of $67.5\ \mu\text{m}$ was formed (Fig. 7e). The resultant length to depth ratio reached a higher value of 2.19 and the entire liquid pool moved slightly toward the opposite direction of the laser beam scanning. Interestingly, the isotherm curves within the molten pool became nonuniformly spaced in this case (Fig. 7c). As the applied P increased to 300 W, the intensified laser energy beam yielded a larger molten pool with length of $209.2\ \mu\text{m}$ and depth of $81.2\ \mu\text{m}$, resulting in a significantly elevated length to depth ratio of 2.57 (Fig. 7e). Moreover, the pool position shifted

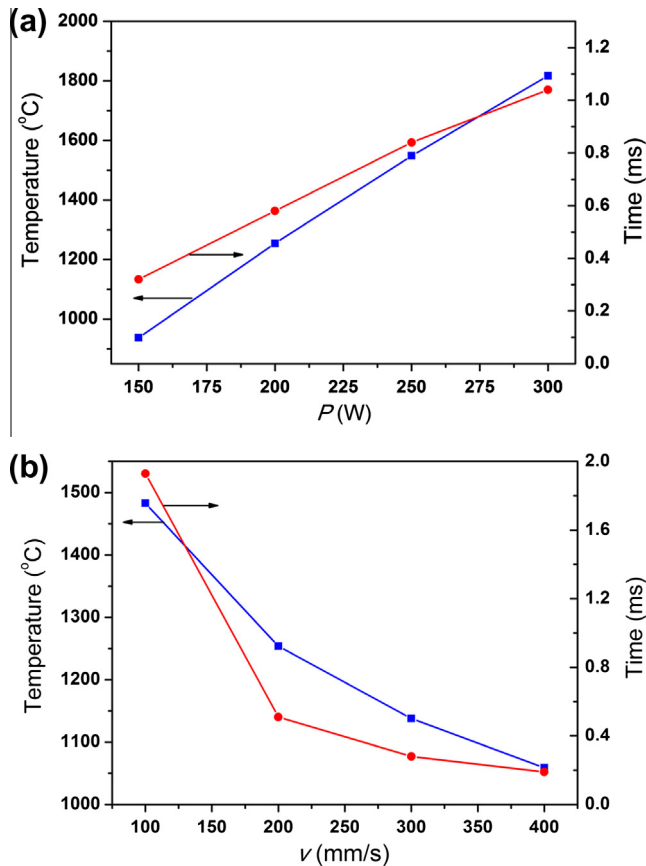


Fig. 5. The maximum temperature and the liquid lifetime during SLM of AlSi10Mg powder process using different laser powers ($v = 200$ mm/s) (a) and different laser scan speeds ($P = 200$ W) (b).

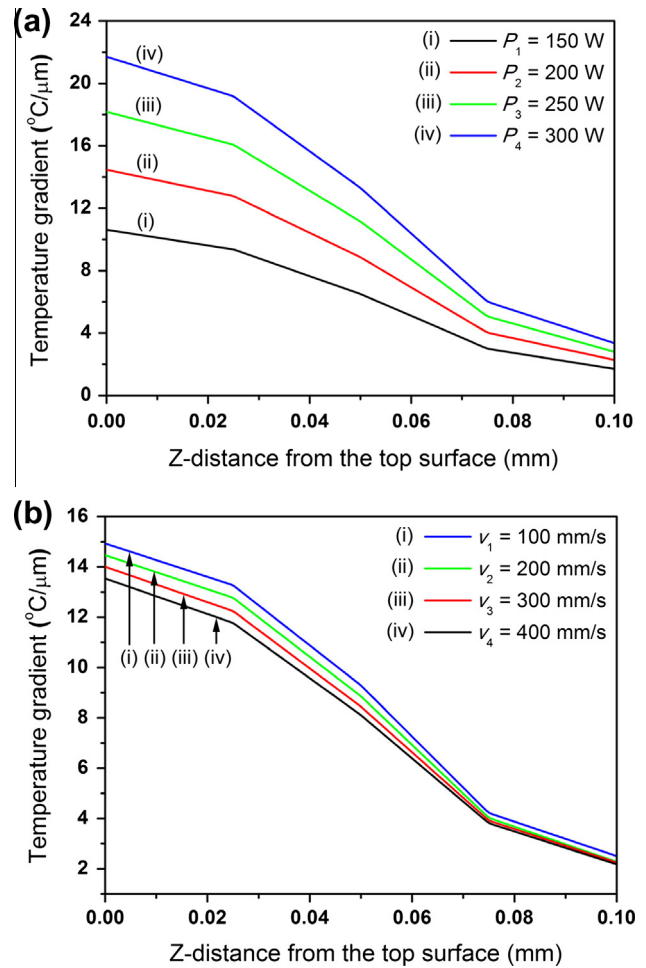


Fig. 6. The variation in the temperature gradient along the depth direction of the molten pool during SLM of AlSi10Mg powder using different laser powers ($v = 200$ mm/s) (a) and different laser scan speeds ($P = 200$ W) (b).

obviously toward the opposite direction of the laser beam scanning.

Fig. 8 shows the change of cross-sectional temperature contours and the length to depth ratio of molten pool with variation of v . It can be seen that the shapes of the liquid pools on the cross-section were similar in various processing conditions though the sizes of which became smaller with applied v increased. At a relatively lower v of 100 mm/s, the molten pool with dimensions of 218.5 μm in length and 99.4 μm in depth was generated after the AlSi10Mg SLM process, and the corresponding length to depth ratio was calculated to be 2.20 (Fig. 8e). The position of the entire molten pool shifted mildly toward the opposite direction of the laser beam scanning. Moreover, it was observed that the isotherms showed a nonuniform distribution characteristic within the molten pool, in which the isotherm curves spaced more closely at the front of the molten pool compared with those at the rear of the molten pool. As the applied v increased to 200 mm/s, the obtained molten pool size decreased to a smaller length value of 103.8 μm and depth of 50.2 μm , and accordingly yielded a lower length to depth ratio of 2.07 (Fig. 8e). In this case, no molten pool position shifts were found, leading to the coincidence between the center line of the molten pool and the axis of the laser beam. Furthermore, the isotherms within the molten pool became regularly and closely spaced (Fig. 8b). On increasing the applied v from 300 mm/s to 400 mm/s, the length and depth of the molten pool gradually shortened whereas the length to depth ratio remained constant at 2.07 (Fig. 8e). The location of the center line of the molten pool and the distribution of the isotherms were essentially identical to those of 200 mm/s (Fig. 8c and d).

As the applied P enhances or v decreases, the size of the cross-section molten pool increases gradually due to the resultant higher laser energy absorption. In order to illustrate the shaping feature of molten pool during the SLM of AlSi10Mg process, the length to depth ratio is introduced. The simulation results manifest that the length to depth ratio of molten pool increases evidently with the enhancement of P , while varies slightly with increment of v . In other words, the morphology of molten pool cross-section is more sensitive to the applied P compared with the utilized v . At a relatively higher P ($P \geq 300$ W) or lower v ($v \leq 100$ mm/s) input, the entire liquid pool tends to shift obviously toward the opposite direction of the laser beam scanning. This can be attributed to the fact that the increased laser energy absorption gives rise to the sufficient volume of melt and accordingly a relatively large solidification zone with higher thermal conductivity as the laser beam moves away. The formation of the larger solidification zone behind the molten pool contributes to the heat transfer during the SLM process, leading to the position shift of the molten pool.

Fig. 9 depicts the effect of P and v on the dimensions of molten pool during SLM of AlSi10Mg powder. As can be seen from the figure, the dimensions of the molten pool were generally in positive linear relation with the applied P . On increasing the applied P from 150 W to 300 W, the increases in the length (from 64.3 μm to 209.2 μm), width (from 55.8 μm to 140.4 μm) and depth (from 33.7 μm to 81.2 μm) of the molten pool were observed (Fig. 9a). As the utilized v increased from 100 mm/s to 400 mm/s, however,

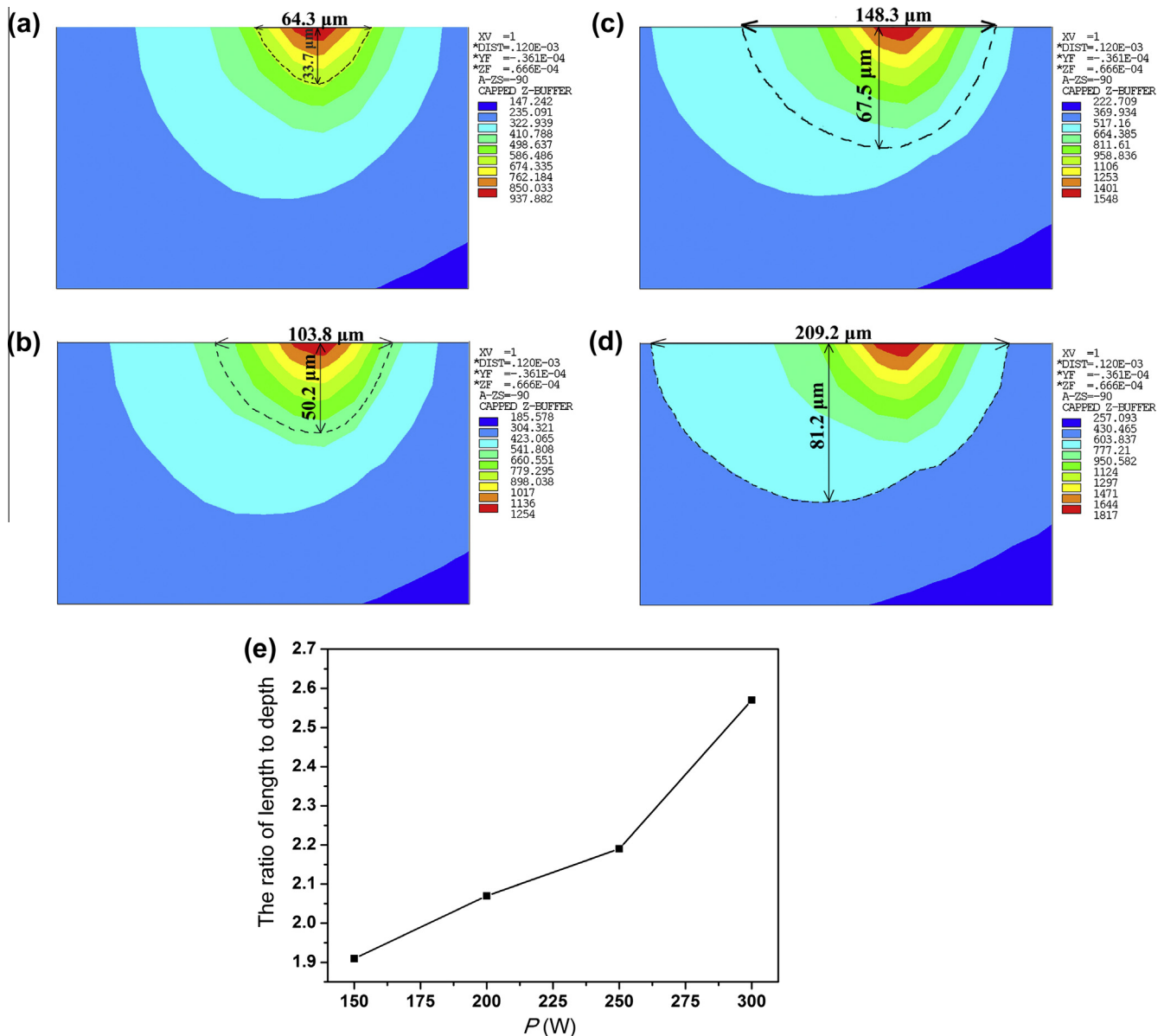


Fig. 7. Temperature distributions on the cross-section of the molten pool during SLM of AlSi10Mg powder at different processing parameters: (a) $P = 150$ W; (b) $P = 200$ W; (c) $P = 250$ W; (d) $P = 300$ W. Variation of the length to depth ratio of the molten pool with the applied laser power (e). Laser scan speed $v = 200$ mm/s is fixed.

the length of the molten pool decreased obviously from 218.5 μm to 73.7 μm . Meanwhile, the width of the molten pool decreased from 168.1 μm to 48.3 μm and the depth of the molten pool reduced from 99.4 μm to 35.2 μm (Fig. 9b). It can be seen that the dimensions of the molten pool decreased with the increment of the applied v during the SLM process, while the decreasing tendency became less pronounced as the applied v increased above 200 mm/s.

Generally, a successful SLM process, characterized by the well bonded adjacent scan tracks and the neighboring layers, should be preformed based on a complete melting and subsequent sufficient solidification process. The density and geometric dimension precision of the SLM-fabricated part are significantly affected by the metallurgical bonding between the adjacent scan tracks and the neighboring layers. It should be noted that the applied P and v play a key role in influencing the metallurgical bonding ability of the SLM-fabricated part. At a relatively higher v of 400 mm/s combined with a constant P of 200 W, a narrow molten pool was obtained with its width size (48.3 μm) slightly less than the hatch

space (50 μm), leading to the poor metallurgical bonding behavior between the adjacent tracks. As the combination of P of 200 W and v of 200 mm/s is utilized, the obtained molten pool depth (50.2 μm) is approximately equal to that of the powder layer thickness (50 μm), resulting in a relatively weak metallurgical bonding between the adjacent layers. As the utilized P lower than 200 W or v higher than 200 mm/s, the laser penetration depth is found to be less than the powder layer thickness. Thereby, the neighboring layers cannot be well bonded since the required overlap rate between the present layer and the previously melt layer cannot be achieved. It thus can be concluded that under the above mentioned laser processing conditions, the SLM-fabricated part with high density and excellent mechanical properties cannot be obtained.

4.4. Experimental investigation

In order to study the layer-by-layer bonding properties of the finished AlSi10Mg samples, the typical etched cross-sectional metallographic microstructures of the shaped samples at different

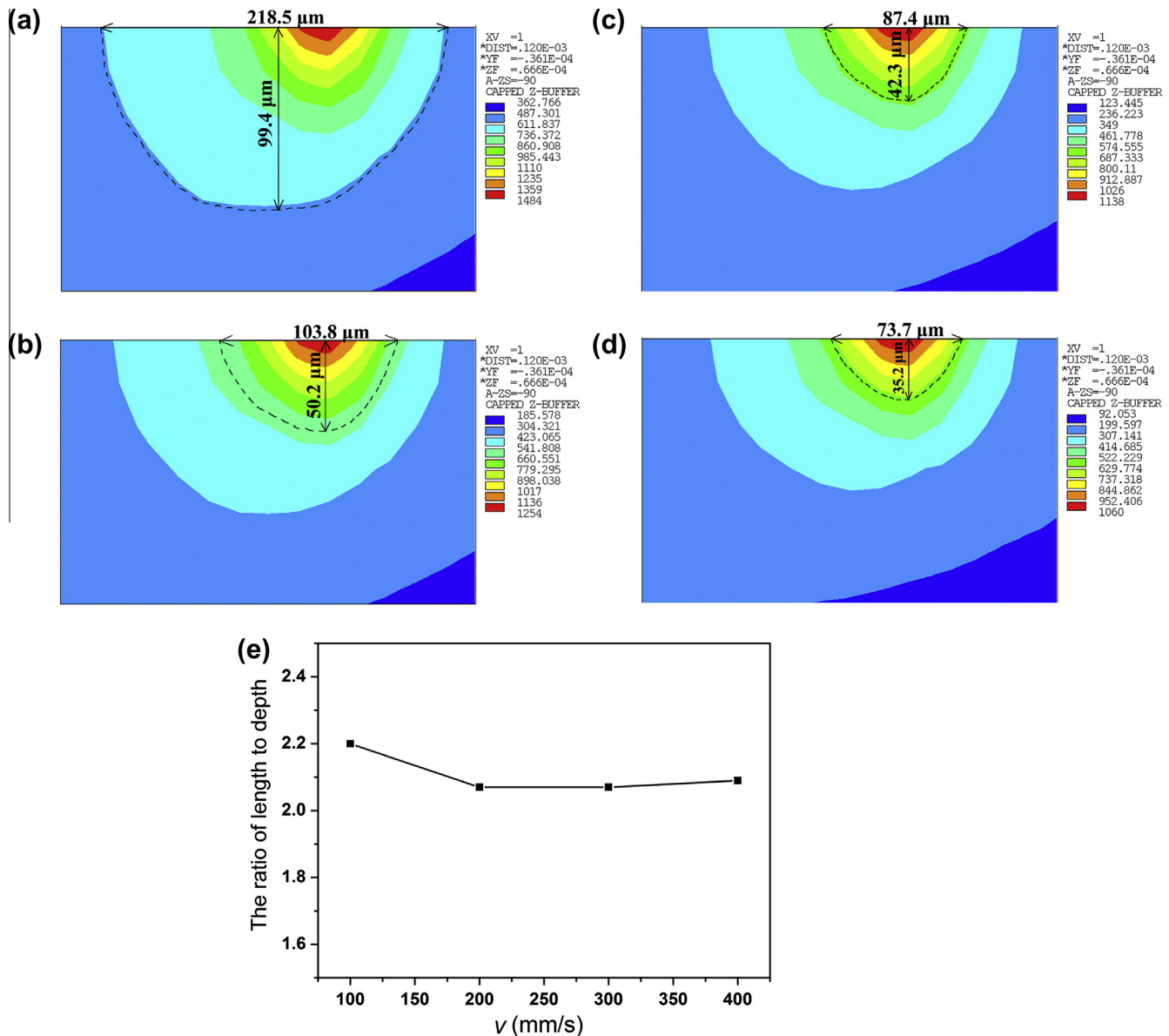


Fig. 8. Temperature distributions on the cross-section of the molten pool during SLM of AlSi10Mg powder at different processing parameters: (a) $v = 100$ mm/s; (b) $v = 200$ mm/s; (c) $v = 300$ mm/s; (d) $v = 400$ mm/s. Variation of the length to depth ratio of the molten pool with the applied laser scan speed (e). Laser power $P = 200$ W is fixed.

P are shown in Fig. 10. Layerwise microstructural features were generally observed as a result of the layer-by-layer fashion of SLM process. At a lower P of 150 W, the larger-sized crescent-shaped pores which crossed over several layers were observed (Fig. 10a). On increasing the input P to 200 W, irregular shaped micropores were found to be dispersed within interlayer bonding areas on the cross-section of the SLM-processed part (Fig. 10b). On further increasing the applied P to 250 W, the dense cross-sectional morphology free of any apparent pores was formed, showing a favorable inter-layer bonding response (Fig. 10c).

During the SLM process, the dynamic viscosity of a molten pool consisting an entirely liquid formation is temperature-dependent [38,39]. The higher operative temperature within a molten pool gives rise to large amount of liquid formation with lower viscosity, which in turn promotes the liquid phase spreading out and improves the metallurgical bonding ability between the neighboring layers. In view of the above experimental results analyses, it

can be found that the metallurgical bonding ability experienced significant changes with different P inputs. At a lower P of 150 W, a considerably small amount of AlSi10Mg liquid is formed due to the lower temperature of 937 °C and shallower laser penetration depth of 33.7 μm (Fig. 5a, Fig. 9a), by which large-sized pores between layers and the resultant poor metallurgical bonding behavior between adjacent layers are inevitably formed (Fig. 10a). On increasing the applied P to 200 W, the volume of the AlSi10Mg liquid phase formation increases, which is believed to be caused by the enhancement of molten pool temperature of 1254 °C (Fig. 5a). In this instance, larger-sized pores alleviated due to more liquid filling and spreading (Fig. 10b). At an even higher P of 250 W, a sufficient amount of liquid phase with low viscosity is produced due to a high temperature of 1548 °C (Fig. 5a). The smoothly spread liquid phase and larger molten pool depth guaranteed the sound metallurgical bonding capacity between the neighboring layers and the resultant higher densification level.

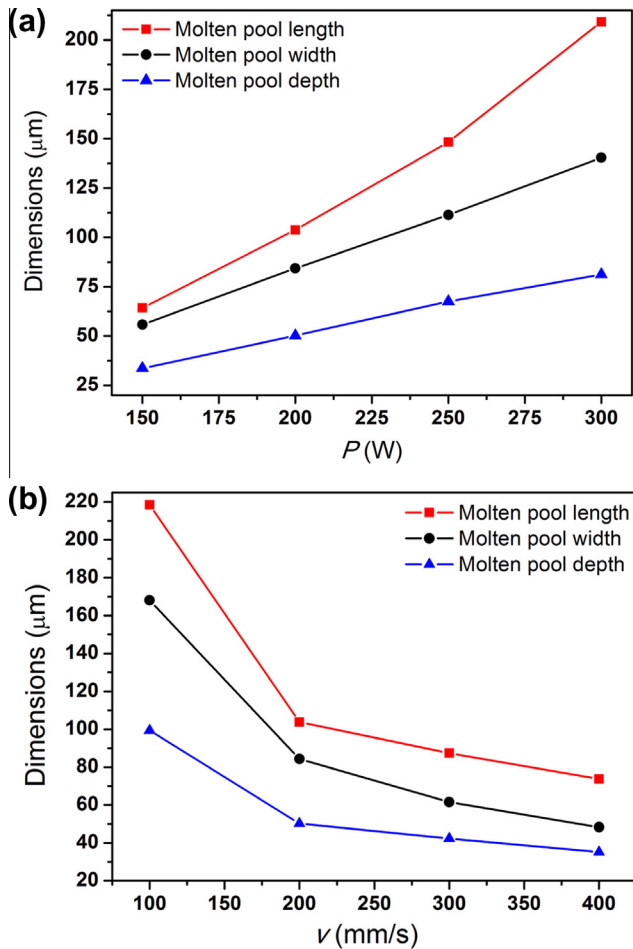


Fig. 9. The dimensions of the molten pool during SLM of AlSi10Mg powder using different laser powers ($v = 200$ mm/s) (a) and different laser scan speeds ($P = 200$ W) (b).

Fig. 11 elucidates that the typical surface morphologies of SLM-produced samples using different v . At a relatively high v of 400 mm/s, an inferior surface quality characterized by large gaps and pores formed along the scanning direction was obtained on the solidified surface, which restricted the densification response to a great extent (Fig. 11a). As the applied v decreased to 300 mm/s, small amount of pores were still present on the solidified surface even though the gaps between the adjacent scan lines disappeared and large areas of dense surface was obtained (Fig. 11b). On further decreasing v to 200 mm/s, a near-full dense and comparatively smooth surface was obtained, showing the formation of stable and continuous tracks and coherent inter-track bonding behavior (Fig. 11c).

During the line-by-line SLM process, the metallurgical bonding ability between the adjacent tracks plays a significant role in influencing the densification behavior of the SLM-produced component. At a relatively higher v of 400 mm/s, a small amount of AlSi10Mg liquid phase with a relatively high viscosity was yielded, due to the lower operative temperature of 1059 °C and the excessively short liquid lifetime of 0.19 ms (Fig. 5b). This inhibited the formed liquid from spreading out smoothly between the adjacent scan tracks, which in turn produced a narrower molten pool width of 48.3 μm compared with the hatch spacing (50 μm) (Fig. 9b). As a consequence, large gaps and pores are observed along the scanning direction after laser melting (Fig. 11a). As the applied v decreases to 300 mm/s, the increasing volume of AlSi10Mg liquid formation and the larger molten pool width of 61.5 μm give rise to the improvement of the inter-track bonding and the elevated densification response (Fig. 11b). On further decreasing the applied v to 200 mm/s, the higher temperature of 1254 °C promotes the formation of sufficient amount of AlSi10Mg liquid phase with appropriate viscosity and attendant good flow ability (Fig. 5b), yielding a wider molten pool width of 84.3 μm (Fig. 9b). The sound inter-track bonding and fully dense surface are thus achieved on the SLM-produced samples (Fig. 11c).

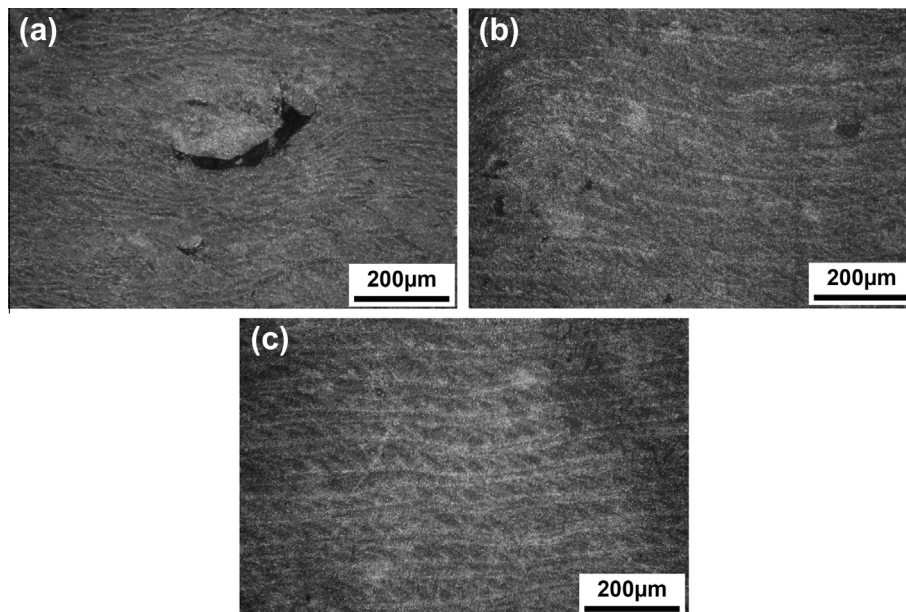


Fig. 10. OM micrographs showing low-magnification microstructures on the etched cross-sections of AlSi10Mg samples at different processing parameters: (a) $P = 150$ W; (b) $P = 200$ W and (c) $P = 250$ W. Laser scan speed $v = 200$ mm/s is fixed.

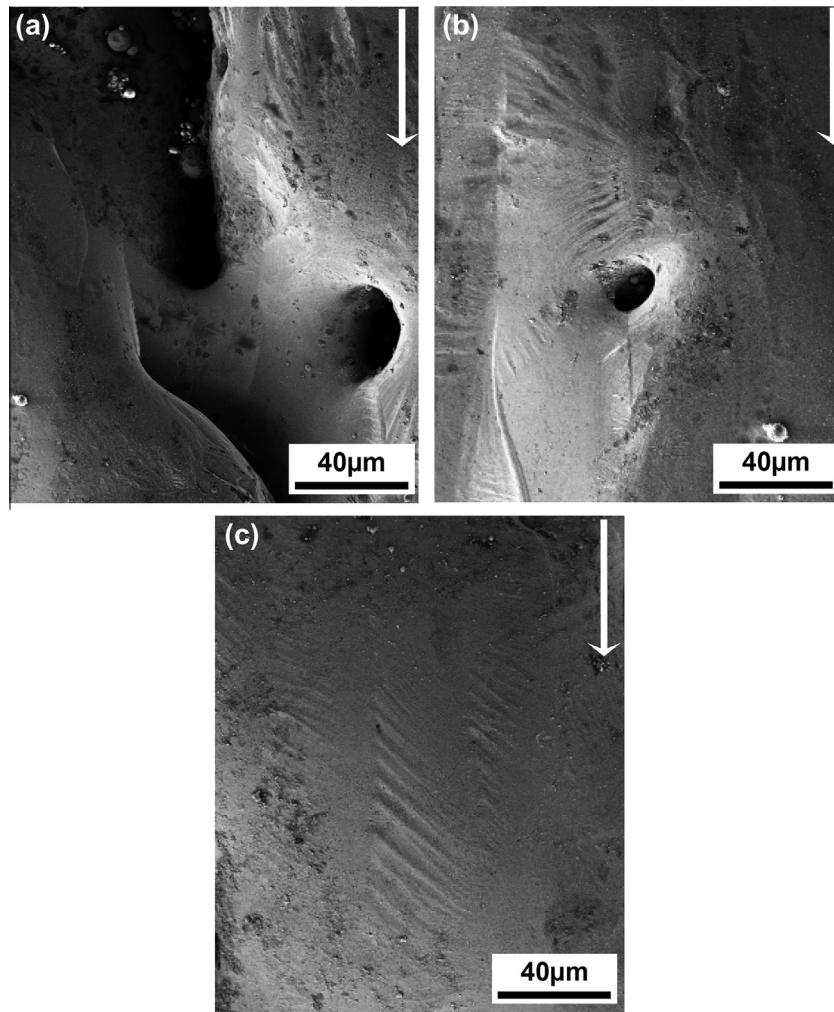


Fig. 11. SEM images showing typical surface morphologies of SLM-processed AlSi10Mg samples at different processing parameters: (a) $v = 400$ mm/s; (b) $v = 300$ mm/s; (c) $v = 200$ mm/s. Laser power $P = 200$ W is fixed.

5. Conclusions

The three-dimensional finite element model was established to investigate the effects of laser power and scan speed on the thermal behavior during the SLM process. Furthermore, the SLM experiments were also conducted in this study, setting the same processing parameters as those used in the simulation. The following conclusions were drawn.

- (1) The maximum temperature, the length, the width, and the depth of the molten pool increased by 4.3%, 12.9%, 15.4%, and 8.5%, respectively, as the laser beam moved from the center of the first layer to the center of the second layer. This is mainly due to the heat accumulation phenomenon and the higher energy losses through the conduction than convection/radiation during the SLM process.
- (2) The cooling rate of molten pool elevated slightly from 2.13×10^6 °C/s to 2.97×10^6 °C/s as the P increased from 150 W to 300 W, while it enhanced significantly from 1.25×10^6 °C/s to 6.17×10^6 °C/s as the v increased from 100 mm/s to 400 mm/s.
- (3) The temperature gradient along the depth direction of the molten pool (Z-direction) gradually decreased as the distance from the top of the molten pool increased. Moreover, the maximum temperature gradient increased considerably (from 10.6 °C/μm to 21.7 °C/μm) as the P elevated from

150 W to 300 W, while it decreased slightly (from 14.9 °C/μm to 13.5 °C/μm) as the v increased from 100 mm/s to 400 mm/s.

- (4) The dimensions of molten pool increased (length: from 64.3 μm to 209.2 μm, width: from 55.8 μm to 140.4 μm, depth: from 33.7 μm to 81.2 μm) as the P elevated from 150 W to 300 W, while decreased (length: from 218.5 μm to 73.7 μm, width: from 168.1 μm to 48.3 μm, depth: from 99.4 μm to 35.2 μm) as the v elevated from 100 mm/s to 400 mm/s. The proper molten pool width (111.4 μm) and depth (67.5 μm) were obtained for a successful SLM process at the combination of P of 250 W and v of 200 mm/s.
- (5) SLM of AlSi10Mg powder was also experimentally performed using different laser processing conditions. A sound metallurgical bonding between the neighboring layers was obtained at the optimized combination of $P = 250$ W and $v = 200$ mm/s, due to the larger molten pool depth (67.5 μm) compared with the powder layer thickness (50 μm).

Acknowledgments

We gratefully appreciate the financial support from the National Natural Science Foundation of China (Nos. 51322509 and 51104090), the Outstanding Youth Foundation of Jiangsu

Province of China (No. BK20130035), the Program for New Century Excellent Talents in University (No. NCET-13-0854), the Program for Distinguished Talents of Six Domains in Jiangsu Province of China (No. 2013-XCL-028), the Science and Technology Support Program (The Industrial Part), Jiangsu Provincial Department of Science and Technology of China, the Fundamental Research Funds for the Central Universities (No. NE2013103), and the Qing Lan Project, Jiangsu Provincial Department of Education of China.

References

- [1] Thijs L, Kempen K, Kruth JP, Humbeeck JV. Fine-structured aluminium products with controllable texture by selective laser melting of pre-alloyed AlSi10Mg powder. *Acta Mater* 2013;61:1809–19.
- [2] Brandl E, Heckenberger U, Holzinger V, Buchbinder D. Additive manufactured AlSi10Mg samples using selective laser melting (SLM): microstructure, high cycle fatigue, and fracture behavior. *Mater Des* 2012;34:159–69.
- [3] Lavernia EJ, Ayers JD, Srivatsan TS. Rapid solidification processing with specific application to aluminium alloys. *Int Mater Rev* 1992;37:1–44.
- [4] Kruth JP, Levy G, Klocke F, Child THC. Consolidation phenomena in laser and powder-bed based layered manufacturing. *CIRP Ann-Manuf Technol* 2007;56:730–59.
- [5] Gu DD, Meiners W, Wissenbach K, Poprawe R. Laser additive manufacturing of metallic components: materials, processes and mechanisms. *Int Mater Rev* 2012;57:133–64.
- [6] Zhang BC, Liao HL, Coddet C. Effects of processing parameters on properties of selective laser melting Mg–9% Al powder mixture. *Mater Des* 2012;34:753–8.
- [7] Zhang BC, Dembinski L, Coddet C. The study of the laser parameters and environment variables effect on mechanical properties of high compact parts elaborated by selective laser melting 316L powder. *Mater Sci Eng, A* 2013;584:21–31.
- [8] Fischer P, Romano V, Weber HP, Karapatis NP, Boillat E, Glatton R. Sintering of commercially pure titanium powder with a Nd:YAG laser source. *Acta Mater* 2003;51:1651–62.
- [9] Gu DD, Wang HQ, Zhang GQ. Selective laser melting additive manufacturing of Ti-based nanocomposites: the role of nanopowder. *Metall Mater Trans A* 2014;45:464–76.
- [10] Das M, Balla VK, Basu D, Bose S, Bandyopadhyay A. Laser processing of SiC-particle-reinforced coating on titanium. *Scripta Mater* 2010;63:438–41.
- [11] Gu DD, Shen YF, Yang JL, Wang Y. Effects of processing parameters on direct laser sintering of multicomponent Cu based metal powder. *Mater Sci Technol* 2006;22:1449–55.
- [12] Ghosh SK, Saha P. Crack and wear behavior of SiC particulate reinforced aluminium based metal matrix composite fabricated by direct metal laser sintering process. *Mater Des* 2011;32:139–45.
- [13] Roberts IA, Wang CJ, Esterlein R, Stanford M, Mynors DJ. A three-dimensional finite element analysis of the temperature field during laser melting of metal powders in additive layer manufacturing. *Int J Mach Tools Manuf* 2009;49:916–23.
- [14] Childs THC, Hauser C. Raster scan selective laser melting of the surface layer of a tool steel powder bed. *Proc Inst Mech Eng Part B: J Eng Manuf* 2005;219:379–84.
- [15] Gusarov AV, Yadroitsev I, Bertrand P, Smurov I. Heat transfer modelling and stability analysis of selective laser melting. *Appl Surf Sci* 2007;254:975–9.
- [16] Gusarov AV, Smurov I. Two-dimensional numerical modelling of radiation transfer in powder beds at selective laser melting. *Appl Surf Sci* 2009;255:5595–9.
- [17] Gusarov AV, Smurov I. Modeling the interaction of laser radiation with powder bed at selective laser melting. *Phys Procedia* 2010;5:381–94.
- [18] Zhang YW, Faghri A, Buckley CW, Bergman TL. Three-dimensional sintering of two-component metal powders with stationary and moving laser beams. *J Heat Transfer* 2000;122:150–8.
- [19] Chen TB, Zhang YW. Numerical simulation of two-dimensional melting and resolidification of a two-component metal powder layer in selective laser sintering process. *Numer Heat Transfer, Part A* 2004;46:633–49.
- [20] Chen TB, Zhang YW. Thermal modeling of laser sintering of two-component metal powder on top of sintered layers via multi-line scanning. *Appl Phys A* 2007;86:213–20.
- [21] Carslaw HS, Jaeger JC. *Conduction of Heat in Solids*. 2nd ed. Oxford: Oxford University Press; 1986.
- [22] Hussein A, Hao L, Yan C, Everson R. Finite element simulation of the temperature and stress fields in single layers built without-support in selective laser melting. *Mater Des* 2013;52:638–47.
- [23] Dai K, Shaw L. Finite element analysis of the effect of volume shrinkage during laser densification. *Acta Mater* 2005;53:4743–54.
- [24] Yin J, Zhu HH, Ke L, Lei WJ, Dai C, Zuo DL. Simulation of temperature distribution in single metallic powder layer for laser micro-sintering. *Comput Mater Sci* 2012;53:333–9.
- [25] Louvis E, Fox P, Sutcliffe CJ. Selective laser melting of aluminium components. *J Mater Process Technol* 2011;211:275–84.
- [26] Rombouts M, Froyen L, Gusarov AV, Bentefour EH, Glorieux C. Light extinction in metallic powder beds: correlation with powder structure. *J Appl Phys* 2005;98:013533.
- [27] Thummler F, Oberacker R. *An Introduction to Powder Metallurgy*. 1st ed. London: The University Press; 1993.
- [28] Touloukian YS, Powell RW, Ho CY, Klemens PG. *Thermophysical properties of matter: thermal conductivity-metallic elements and alloy*. 1st ed. New York: IFI/Plenum; 1970.
- [29] Touloukian YS, Buyco EH. *Thermophysical properties of matter: specific heat-metallic elements and alloy*. 1st ed. New York: IFI/Plenum; 1970.
- [30] Alimardani M, Toyserkani E, Huisoon JP, Paul CP. On the delamination and crack formation in a thin wall fabricated using laser solid freeform fabrication process: an experimental–numerical investigation. *Opt Lasers Eng* 2009;47:1160–8.
- [31] Zheng B, Zhou Y, Smugeresky JE, Schoenung JM, Lavernia EJ. Thermal behavior and microstructural evolution during laser deposition with laser-engineered net shaping: Part I. Numerical calculations. *Metall Mater Trans A* 2008;39:2228–36.
- [32] Yadroitsev I, Gusarov A, Yadroitsava I, Smurov I. Single track formation in selective laser melting of metal powders. *J Mater Process Technol* 2010;210:1624–31.
- [33] Gu DD, Hagedorn YC, Meiners W, Meng GB, Batista RJS, Wissenbach K, et al. Densification behavior, microstructure evolution, and wear performance of selective laser melting processed commercially pure titanium. *Acta Mater* 2012;60:3849–60.
- [34] Gu DD, Shen YF. Balling phenomena in direct laser sintering of stainless steel powder: metallurgical mechanisms and control methods. *Mater Des* 2009;30:2903–10.
- [35] Simchi A, Pohl H. Effects of laser sintering processing parameters on the microstructure and densification of iron powder. *Mater Sci Eng A* 2003;359:119–28.
- [36] Dai DH, Gu DD. Thermal behavior and densification mechanism during selective laser melting of copper matrix composites: simulation and experiments. *Mater Des* 2014;55:482–91.
- [37] Liu FC, Lin X, Huang CP, Song MH, Yang GL, Chen J, et al. The effect of laser scanning path on microstructures and mechanical properties of laser solid formed nickel-base superalloy Inconel 718. *J Alloys Compd* 2011;509:4505–9.
- [38] Fischer P, Romano V, Weber HP, Karapatis NP, Boillat E, Glatton R. Sintering of commercially pure titanium powder with a Nd:YAG laser source. *Acta Mater* 2003;51:1651–62.
- [39] Yadroitsev I, Bertrand P, Smurov I. Parametric analysis of the selective laser melting process. *Appl Surf Sci* 2007;253:8064–9.